Hybrid silicon-conductive oxide-plasmonic electro-absorption modulator with 2-V swing voltage

Qian Gao
Erwen Li
Bokun Zhou
Alan X. Wang

SPIE.

Hybrid silicon-conductive oxide-plasmonic electro-absorption modulator with 2-V swing voltage

Qian Gao, Erwen Li, Bokun Zhou, and Alan X. Wang*
Oregon State University, School of Electrical Engineering and Computer Science,
Corvallis, Oregon, United States

Abstract. Transparent conductive oxides (TCOs) have emerged as materials for nanoscale electro-optic modulators. The free-carrier-induced epsilon-near-zero effect by applying a gate voltage is capable of achieving ultra-strong electro-absorption (EA) effect. As the EA rate has been theoretically proved to be dependent on the mobility of the TCO gate, we experimentally demonstrated a hybrid silicon-plasmonic EA modulator using high-mobility In_2O_3 as the gate. With an ultra-compact active region of only 5-μm long, we achieved a small voltage swing V_{pp} of only 2 V to obtain an EA rate of 1.2 dB/μm, resulting in very high energy efficiency of 110 femto-joule/bit. We also experimentally proved the correlation between the EA rate and the mobility of TCO materials through comparison with indium-tin-oxide gated modulators. In addition, the hybrid EA modulator is capable of covering more than 100-nm optical bandwidth in the telecommunication wavelength window, which is limited by the bandwidth of the grating coupler. © *2019 Society of Photo-Optical Instrumentation Engineers (SPIE)* [DOI: 10.1117/1 .JNP.13.036005]

Keywords: silicon photonics; transparent conductive oxides; modulator; epsilon-near-zero material.

1 Introduction

Various emerging photonic materials, such as grapheme,[1] electro-optic polymer,[2] and phase change materials,[3] have been integrated with silicon photonics in recent years. Transparent conductive oxides (TCOs), including indium tin oxide (ITO), indium oxide (In_2O_3), and aluminum zinc oxide, have also attracted escalating research interests in integrated photonic devices[4,5] and metamaterials/metasurfaces[6] due to the epsilon-near-zero (ENZ) effect, when the real permittivity crosses the zero point in the near- to mid-infrared wavelength, depending on the free-carrier concentration. The relationship between the permittivity and the free-carrier concentration can be obtained by the Drude model.[7] At 1.55-μm wavelength, the real permittivity of TCOs reaches zero while the absolute value of the optical permittivity is at the minimum value due to the small imaginary part when the free-carrier concentration is around $6.4 \times 10^{20}/cm^3$. Such unique optical properties, namely ENZ,[8] will dramatically enhance the light–matter interaction. The extraordinary nonlinear optical effect[9] and the large perturbation to the refractive indices[10] at the ENZ wavelength have been achieved either through oxygen vacancy doping[11] or electrical gating.[12] In addition, TCO materials can be easily deposited with high quality to achieve long-term stability. DC- or RF-sputtering[13] is one of the most widely used methods to deposit TCO materials, which allows high deposition rates, good reproducibility, and the possibility of scaled manufacturing using commercially available large area sputtering systems. Meanwhile, sputtering can achieve a large tunability of the electrical and optical properties by varying deposition conditions in the process. As a comparison, other TCO deposition techniques, such as chemical vapor deposition, generally face difficulties of finding volatile and thermally stable source materials.[14] For thermal evaporation, the challenge comes from controlling the composition of the liquid alloy due to the different vapor pressure of metal elements.[15] Pulsed laser deposition is

---

another effective technique to deposit high-quality TCO materials with good control of the composition and material properties. However, the expensive equipment cost and the slow deposition rate make it unsuitable for scalable manufacturing.[16]

In the past years, several groups have designed[8,17–19] and demonstrated[20–23] ultra-compact electro-absorption (EA) modulators with TCO gates utilizing the ENZ effect. In such devices, applying the gate voltage will induce a thin layer (~1 nm) of accumulated electrons in the TCO materials, which turns the dielectric-like material into ENZ, causing ultra-high light concentration and absorption in the accumulation layer. It has been theoretically proved that the EA rate of the modulator depends on the mobility of the TCO material[24] since higher mobility TCO will cause stronger optical field concentration in the ENZ layer, and therefore, higher extinction ratio (ER) can be achieved with the same voltage swing V_{pp} applied to the gate. In this paper, we used a high mobility In_2O_3 gate to replace low mobility ITO, which is integrated on a silicon-on-insulator (SOI) waveguide to lower the voltage swing of the hybrid EA modulator. The high mobility In_2O_3 EA modulators were experimentally demonstrated with higher ER than the low mobility ITO modulators using the same voltage swing. For high mobility In_2O_3 EA modulators, we experimentally achieved a small voltage swing V_{pp} of only 2 V to obtain an ER of 1.2 dB/μm, resulting in very high energy efficiency of 110 femto-joule/bit (fJ/bit). Finally, the hybrid EA modulator is capable of covering more than 100-nm optical bandwidth in the telecommunication wavelength window and 55-MHz RC-delay limited bandwidth.

2 Device Design and Quantum Modeling

The design of the silicon EA modulator with In_2O_3 gate is depicted in Fig. 1(a). The proposed modulator operates at the 1.55-μm telecom wavelength consisting of a silicon strip waveguide (width $\times$ height $= 450 \times 250$ nm^2). The EA region is deposited with a 10-nm thick HfO$_2$ layer, 20-nm In_2O_3 layer, and 100-nm Au Layer. Light is coupled into and out of the waveguide through two grating couplers.[25] In the active EA region, as shown in Fig. 1(b), In_2O_3-HfO$_2$-Si forms a metal-oxide-semiconductor (MOS) capacitor. The HfO$_2$ serves as the gate insulator with high dielectric constant. The Au film on top of the In_2O_3 layer acts simultaneously as the top electrode and the plasmonic layer to guide and confine the plasmonic waveguide mode inside the active region. The silicon waveguide serves as the bottom electrode, which was moderately doped to 1×10^{17}/cm^3 to reduce the series resistance. Two 400-nm wide silicon strips are used to form the conduction path between the silicon waveguide and the silicon contacting region with Al electrodes, as shown in Fig. 1(a). Standard ground-signal-ground (GSG) electrode pads were designed as 50 Ω coplanar waveguide so that the impedance of the GSG electrodes matches that from the RF cable to minimize the reflection. The width ratio of the ground, signal, and ground pad is 5:4:5, and this ratio is constant from the probe contacting region to the device. The total length of the on-chip coplanar waveguide electrodes is 300 μm.

In_2O_3 modulators employ the plasma dispersion effect and the ENZ enhancement to induce optical absorption. Maximal optical transmission occurs without an electrical bias, which is defined as the "ON state." The optical transmission can be modulated by applying a negative gate bias ($-V_{gate}$) between the electrodes to induce accumulation layers at the In_2O_3/HfO$_2$ and HfO$_2$/p-Si interfaces, causing a strong perturbation to the complex permittivity of the In_2O_3 and
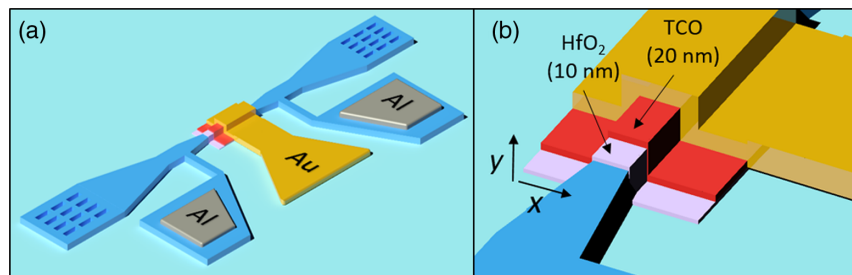
Fig. 1 (a) The 3-D schematic of the hybrid silicon-plasmonic EA modulator with In_2O_3. (b) The zoomed-in view of the Si/HfO$_2$/In_2O_3/Au MOS capacitor at the center of the EA modulator.

Si layers by reducing the real part and increasing the imaginary part of the optical permittivity. The ENZ effect in the In_2O_3 layer induces a large field enhancement and enables a strong EA enhancement. We define this high absorption state as the "OFF" state. The switching behavior of the EA modulator is based on the carrier effect in the ultra-thin accumulation layer. A quantum model is widely used to solve the problems of thin gate oxide MOS devices under a strong electric field. In order to turn the TCO material into the ENZ state, a thin high dielectric constant gate insulator layer is necessary. Therefore, a narrow and deep potential well is formed at the interface with a high gate voltage, which matches the quantum model condition very well. According to the quantum mechanics theory, in such a narrow triangular potential well, the kinetic energy of the carriers in the direction perpendicular to the surface is quantized. In our paper, we used to the density gradient model[26] to solve the carrier distribution, which is available in Silvaco EDA™.

3 Optical Simulation

The relationship between the carrier density and the permittivity of In_2O_3 $\varepsilon_r = \varepsilon_1 + i\varepsilon_2$ is modeled by the Drude model.[7]

$$\varepsilon_r = \varepsilon_\infty + \frac{\omega_p^2}{[\omega(\omega + i\Gamma)]},$$ (1)

where $\varepsilon_\infty = 3.9$ is the high frequency dielectric constant and ω_p is the plasma frequency defined as follows:

$$\omega_p^2 = \frac{N_c q^2}{\varepsilon_0 m^*},$$ (2)

and Γ is the plasma collision frequency, which is given by

$$\Gamma = q/(\mu m^*).$$ (3)

Here, N_c is the carrier concentration, q is the electron charge, ε_0 is the vacuum permittivity, μ is mobility, and $m* = 0.35m_e$ is the effective mass of the free carrier. Using the Drude model, we can obtain the relationship between the absolute value of epsilon and the free-carrier concentration. The free-carrier concentration (n) for ENZ is calculated when the absolute value of epsilon is the lowest. For In_2O_3, the measured mobility is 32 cm^2/V · s. At 1.55-μm wavelength, the ENZ condition corresponds to a total carrier concentration $n = n_0 + \Delta n_{acc} = 6.4 \times 10^{20}$ cm^{-3}, where n_0 is the bulk carrier concentration in In_2O_3 and Δn_{acc} is accumulated electrons, the real part of the accumulation layer's permittivity approaches zero. Physically, this represents a material transition from a dielectric response to a metallic response at 1.55-μm wavelength, namely, the ENZ point. ENZ materials induce extraordinary optical field enhancement as results of the continuity of normal component of the electric displacement field. The electric field enhancement, $|E_{ENZ}/E_{HfO2}| = |\varepsilon_{HfO2}|/|\varepsilon_{ENZ}|$, in an ENZ material is proportional to $1/|\varepsilon_{ENZ}|$, where ε_{HfO2} and E_{HfO2} are the permittivities of the electric field inside the oxide. The upper bound of this field enhancement is governed by how small $|\varepsilon_{ENZ}|$ can be, which itself is determined by how large the free-carrier mobility of ENZ material can be. Therefore, the mobility of the TCO material plays an important role to determine the ER of EA modulators.[24]

We sputtered both In_2O_3 and ITO film and measured the mobility and carrier concentration by the Hall measurement. The results show that In_2O_3 has relatively high mobility of 32 cm^2/V · s compared to typical ITO film of 15 cm^2/V · s. The mode profile of the hybrid Au-Si waveguide and the propagation loss can be derived by incorporating the permittivity into Lumerical MODE solver. The hybrid plasmonic/photonic waveguide mode, as shown in Fig. 2(a), resides largely in the thin In_2O_3 and gate dielectric layer. The mode profile is calculated under transverse-electric (TE) excitation with a dominant electric field component along the x direction. The "OFF" state of the mode profile is shown in Fig. 2(b). The enlarged view in Fig. 2(b) of the In_2O_3/HfO$_2$ interface shows the field enhancement in the accumulation layer
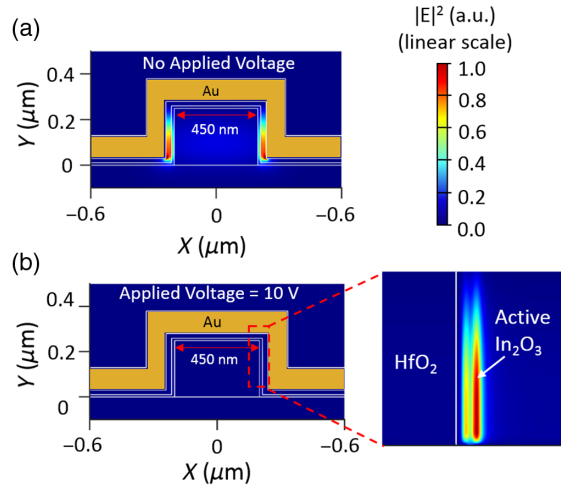
Fig. 2 Simulated optical mode profile for (a) the hybrid Si-Au waveguide with no applied bias and (b) the In_2O_3 hybrid Si-Au waveguide at ENZ when the applied bias is 10 V and the enlarged region of the ENZ In_2O_3 layer.

at "OFF" state, which clearly proves the ultra-strong optical field concentration in the ENZ layer. For 450-nm Au-Si waveguide, the simulated effective index is $2.685 + 0.0182i$ at 0 V and $2.675 + 0.0588i$ at 10 V. The 3× increase of the imaginary part from 0 to 10 V corresponds to the EA rate of the modulator. The slight decrease of the real part from 0 to 10 V proves that more optical field is concentrated into the ENZ In_2O_3 layer from the high refractive index silicon waveguide as shown in the enlarged view in Fig. 2(b) of the In_2O_3/HfO_2 interface.

Next, we compare the "OFF" state ($V_{gate} = 10$ V) of EA modulators with low and high mobility TCO materials. Table 1 summarizes the permittivity of In_2O_3 and ITO at the ENZ state. It shows that $|\varepsilon_{ENZ,In2O3}|$ is closer to zero than $|\varepsilon_{ENZ,ITO}|$ due to the higher mobility. Figure 3(a) shows the $|\varepsilon_{ENZ}|$ distribution of In_2O_3 and ITO at the interface when $V_{gate} = 10$ V. Since $|\varepsilon_{ENZ,In2O3}|$ is closer to zero than $|\varepsilon_{ENZ,ITO}|$, we expect that In_2O_3 have higher field intensity and stronger confinement in the ENZ layer than ITO, which is illustrated in Fig. 3(b).

Table 1 Material parameters for the In_2O_3 and ITO semiconductors.

TCO material	Mobility ($cm^2/V \cdot s$)	Carrier density (cm^{-3})	ε_{ENZ}	$|\varepsilon_{ENZ}|$
ITO	15	6.4×10^{20}	$0.25 + 1.0i$	1.0
In_2O_3	32	6.4×10^{20}	$0.039 + 0.50i$	0.5
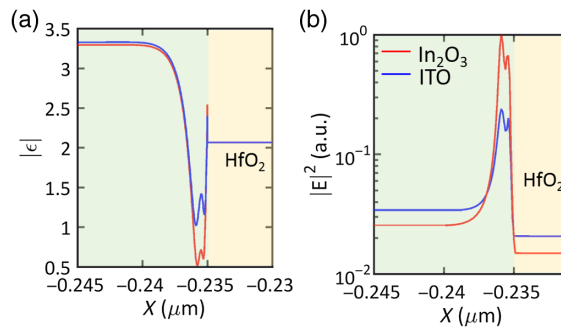
Fig. 3 Zoomed-in view of the absolute value of (a) the optical permittivity and (b) electric field intensity (in log scale) distribution at the TCO/HfO_2 interface obtained by the quantum model for In_2O_3 and ITO gates.

When the mobility is high, the field in the bulk In_2O_3 and HfO_2 is negligible and the field in the ENZ layer is strong. However, for ITO with lower mobility, the field in the ENZ layer is lower and extends into the bulk ITO as well as the HfO_2. Less field overlapping with the ENZ layer will lead to lower EA strength. We need to point out that the EA effect majorly comes from the TCO material while the increasing of the free-carrier concentration in silicon has negligible effects compared to the TCO layer due to two reasons. First, the optical field is highly confined in the accumulation layer in the In_2O_3 layer, as shown in Fig. 3(b). Second, the plasmonic absorption in silicon is only 1/30 of that in TCO materials, as shown in our previous work.[27]

4 Device Fabrication

The fabrication of the hybrid silicon-plasmonic EA modulator starts from a commercial SOI wafer with a 250-nm thick silicon layer and a 3-μm-thick buried oxide layer. The SOI wafer was moderately doped to $1 \times 10^{17}/cm^3$ to reduce the resistivity. The Si waveguide is patterned by electron beam lithography (EBL) and reactive ion etching (RIE) as shown in Fig. 4, steps 1–3. We fabricated hybrid Si-Au waveguide with two different Si waveguide widths (300 and 450 nm). To construct the MOS capacitor in the active region, a 10-nm HfO_2 was deposited by atomic layer deposition (ALD) as the gate oxide as step 4 in Fig. 4. Next, as shown in Fig. 4, steps 5 and 6, the hybrid Si-Au waveguide was patterned by EBL with alignment to the Si strip waveguide, followed by RF sputtering of 20 nm In_2O_3 and thermally evaporating 3-nm-thick Cr as an adhesion layer and 100-nm-thick gold film. Then, the hybrid waveguide was formed through a lift-off process. The as-deposit In_2O_3 with higher O_2 flow has relatively low carrier concentration. A postannealing process was performed in air at 500°C for 5 min to increase the carrier concentration without decreasing the mobility. After that, metal contact on Si (200 nm Al) and Au electrodes was patterned by contact photolithography. To form an ohmic contact between the Al and Si, the sample was annealed at 475°C.

The optical image of the fabricated device with electrode pads is shown in Fig. 5(a). The scanning electron microscopy (SEM) image in Fig. 5(b) shows the hybrid Si-Au waveguide ($L = 5$ μm, $W = 300$ nm) with tapers connected to the Si strip waveguides. The tiled view of the SEM image in Fig. 5(c) shows the $Si/HfO_2/In_2O_3/Au$ in the active region.

In this work, we fabricated multiple devices with different lengths (5, 10, and 15 μm) with the same grating couplers and waveguide tapers. The optical transmission data are plotted in Fig. 6. From the slope of the linear fitted curves, we obtained the propagation loss of the 300- and 450-nm waveguides to be 2.0 and 1.3 dB/μm at 1550-nm wavelength. The total coupling loss for the 300-nm waveguide is 20 dB and the 450-nm waveguide is 16 dB. By excluding the plasmonic waveguide propagation loss, we can obtain the total coupling loss, which includes
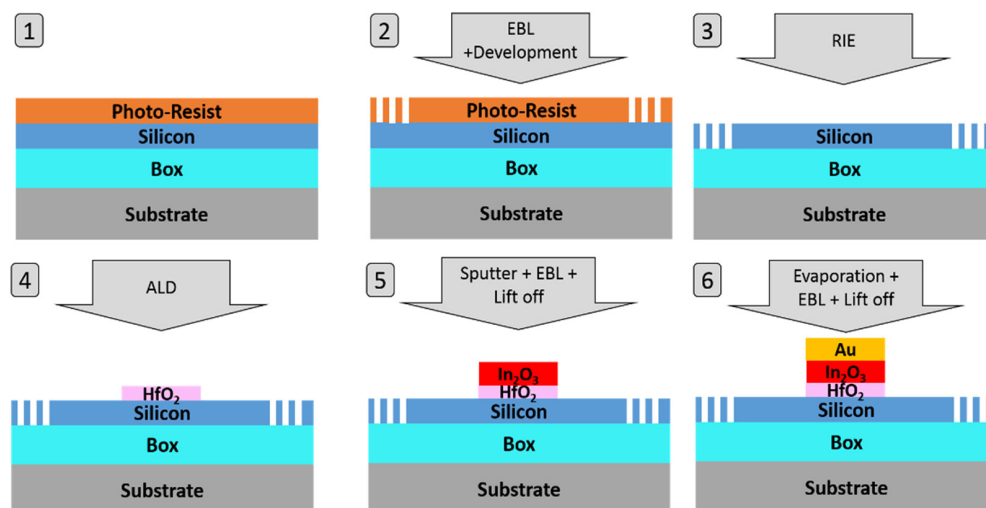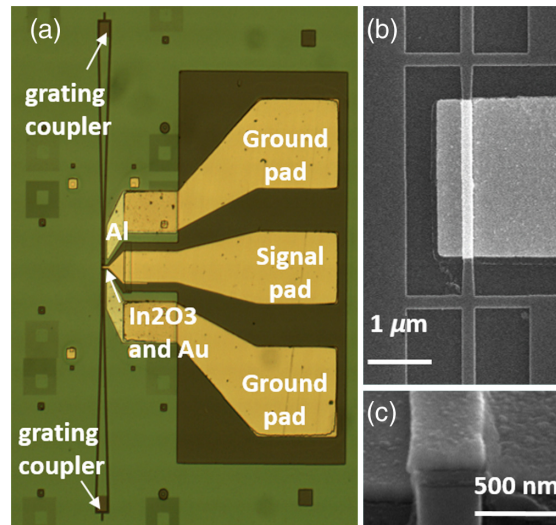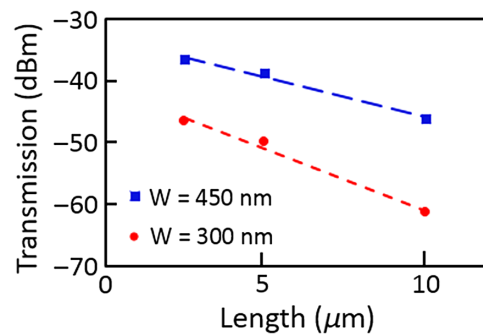

Fig. 4 Fabrication process flow chart for the Si-TCO-plasmonic EA modulators.

Fig. 5 (a) Optical image of the hybrid Si-Au EA modulator, (b) SEM image of the hybrid Si-Au waveguide, and (c) SEM image of the cross-sectional view of the $Si/HfO_2/In_2O_3/Au$ MOS capacitor.


Fig. 6 Optical transmission data of the 300- and 450-nm waveguide with different lengths.

the grating coupler coupling loss, tapering loss, and coupling loss from the Si waveguide to the hybrid plasmonic waveguide. For the 300- and 450-nm waveguides, the grating coupler coupling loss should be the same. The 300-nm-width waveguide, however, has a higher tapering loss and higher coupling loss from Si waveguide to the hybrid plasmonic waveguide compared to the 450-nm waveguide. In addition, the plasmonic waveguide loss of the 300-nm waveguide is also higher. The measurement results show that the narrower waveguide width increases the propagation loss, which matches the simulation results. However, the actual "ON" state loss is higher than the simulation results due to the roughness on waveguide sidewalls induced by the RIE process and the higher optical absorption of the actual Au film compared with that from the bulk material.

5 DC Electro-Optic Modulation

The simulated ER for In_2O_3 and ITO gates in Fig. 7(a) (red solid and red dotted lines) clearly shows that at the "OFF" state, the ER of In_2O_3 of 1.5 dB/μm is higher than that of ITO of 1 dB/μm for 450-nm waveguides. Moreover, the trend of the ER as the V_{gate} is affected by the mobility as well. The ER_{ITO} as a function of V_{gate} is more linear. The ER_{In2O3} increases slower when the V_{gate} is small but starts to take off at higher gate voltage. Another consequence of using TCO materials with lower mobility is that the "ON" state propagation loss will be raised. The above analysis concludes that higher mobility ENZ materials are pivotal to achieve EA
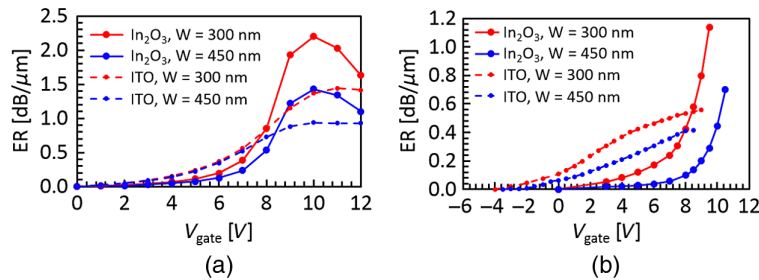
Fig. 7 (a) Simulation results and (b) experimental results of the modulation strength as a function of the gate voltage for In_2O_3 with different waveguide widths.

modulators with higher modulation strength as well as lower "ON" state loss. The modulation strength can also be affected by the Si waveguide width. Reducing the Si waveguide width enhances the lateral confinement of the hybrid plasmonic-photonic mode and more field resides in the low index HfO_2/In_2O_3 layer, therefore, higher ER is expected. It is shown that as the gate voltage increases, the ER gradually increases and reaches the maximum value of 2.2 dB/μm at 10 V for 300-nm waveguide. However, the ER versus V_{gate} is highly nonlinear, and most of the ER increase occurs at 8–10 V. Therefore, it is feasible to drive the EA modulator at a DC bias (at 9 V) with a small voltage swing ($V_{pp} \sim 2$ V). Another interesting phenomenon from the simulation shows that as the voltage goes beyond 10 V, more accumulated free carriers will actually increase the absolute value of epsilon as the real permittivity turns negative. Therefore, the optical field enhancement due to the ENZ effect will degrade, which causes a drop of the ER as the bias voltage is higher than 10 V.

In our experiment, a DC voltage was applied to the signal pads while the bottom silicon connecting to the ground pad was grounded. Solid lines in Fig. 7(b) show the ER of the EA modulator with In_2O_3 material as a function of the applied gate voltage with $W = 300$ nm (red solid line) and 450 nm (blue solid line). The electrically induced absorption slowly accelerates at a lower gate voltage and takes off at higher voltage, which is similar to the simulation results in Fig. 7(a). The ER did not show a clear trend to saturation at $V_{gate} = 10$ V, indicating that the modulation depth could likely be further increased with a larger gate voltage. However, to avoid breakdown of the 10-nm HfO_2 layer, higher gate voltage was not continued. The measurement also verifies that EA modulators with a narrower waveguide width offer higher ER. However, the maximum ER from the measurement, 1.2 dB/μm with $W = 300$ nm and 0.7 dB/μm with $W = 450$ nm, is smaller than the simulation result due to two possible reasons. First, 10-V applied voltage is very close to the breakdown voltage of 10-nm HfO_2. The oxide layer may already have some leakage current due to possible conductive paths.[28] The small leakage current will reduce the accumulated charges at the interface. Second, the fabrication imperfections may lead to defects at the Si waveguide sidewall and the interface between HfO_2 and In_2O_3, which may induce fixed charges and trap electrons, as discussed in Ref. 28. These fixed and trapped charges are resilient to the gate voltage, resulting in smaller EA modulation strength.

To verify the effect of the mobility obtained from simulation, we also fabricated EA modulators using ITO with lower mobility as the gate using the same fabrication process. The as-deposited ITO film under low O_2 level without postannealing process has higher carrier concentration and lower mobility. Electro-optic (E-O) characterization of the devices was performed as well. The experimental ER from the ITO EA modulators as a function of the applied gate voltage with $W = 300$ and 450 nm were compared with In_2O_3 EA modulators, as shown in Fig. 7(b) dashed lines. The trend of the ER as a function of V_{gate} matches our simulation results. The ER of the ITO EA modulator was higher at lower V_{gate} and increased more linearly than the ER of the In_2O_3 modulator. In addition, the modulation strength of the ITO EA modulator is much lower than the In_2O_3 EA modulator at higher gate voltage. It is shown that the measured ER is lower than the simulated ER due to similar reasons, as we discussed for the In_2O_3 EA modulators. A thorough comparison of previous theoretical and experimental results of TCO modulators in terms of driving voltages and EA rates can be found in our recently published paper.[27]
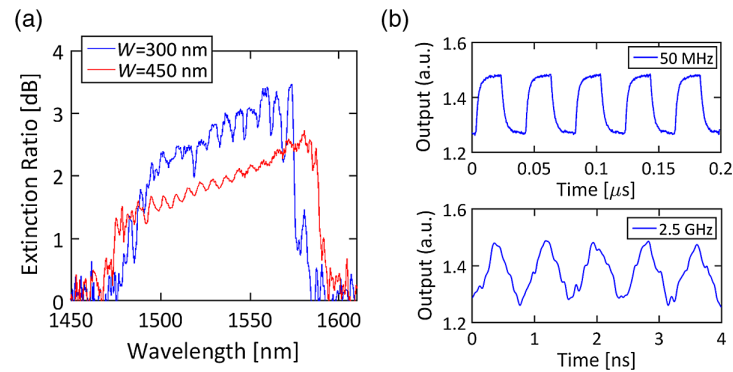
Fig. 8 (a) Measured ER with $V_{\text{gate}} = 9$ V for $L = 5$ μm EA modulators with different waveguide widths. (b) Dynamic optical modulation testing results of the EA modulator with -8 to -10 V sweep input gate voltage at 50 MHz (top) and 2.5 GHz (bottom).

6 AC Testing

We also measured the ER of the 5-μm-long devices with 300- and 450-nm waveguide widths over a broad wavelength range at $V_{\text{gate}} = 9$ V. In Fig. 7(a), we plot the ER of the In_2O_3 EA modulators in the wavelength range of 1450–1650 nm, which shows a 100-nm broadband response. The bandwidth is mainly limited by the coupling efficiency of the grating couplers. In Fig. 8(a), the 300-nm waveguide shows a smaller bandwidth than the 450-nm waveguide. We believe that this was simply caused by the measurement process, which is not intrinsic to the device. As shown in Fig. 6, narrower waveguide induces higher optical loss. Overall, the optical transmission spectrum from the 300-nm waveguide is much lower compared to that of the 450-nm waveguide across the measured wavelength window. Because of the limited bandwidth of the grating couplers, the transmission spectra outside of the high-efficiency window of the grating couplers will approach to the noise level, which poses a measurable bandwidth of the device. Since the transmission spectrum of the 300-nm waveguide is closer to the noise floor, it appears that the bandwidth is narrower. Figure 8(a) also shows that higher ER occurs at longer wavelength because lower carrier density is required to reach the ENZ region at a longer wavelength. In addition, we believe the two waveguide tapers are not perfectly adiabatic and the reflections cause ripples in the transmission spectra. From the resonant condition of a cavity $\Delta\lambda = \lambda^2/(nL)$, the cavity length is calculated to be around 120 μm, which approximately matches the length of the straight waveguide between the two waveguide tapers. Finally, we characterized the high-speed modulation by driving the device with an RF signal across the GSG electrodes and measuring the optical output waveform. A continuous wave generated by a tunable laser source at 1530 nm with TE polarization was coupled to silicon waveguide through the grating coupler. The optical output was amplified by an erbium-doped fiber amplifier and detected by an Agilent digital communication analyzer. The input electric signal was generated with V_{pp} magnitude of 2 V and a -9 V DC bias. The dynamic modulation speed was demonstrated at 50 MHz and 2.5 GHz, as shown in Fig. 8(b). The input signal was a square wave. The output waveform at 50 MHz is very close to a square shape while the output waveform at 2.5 GHz is distorted because 2.5 GHz exceeds the calculated RC-delay limited bandwidth of the device.

We calculate the bandwidth of the device based on the optical rise time (10%–90%) of 6.5 ns, which corresponds to a 3-dB bandwidth of 55 MHz. The estimated capacitance of the 5-μm long active region is $C = 0.11$ pF, which correspond to 110-fJ/bit energy consumption using $CV_{\text{pp}}^2/4$. In this article, we only compare broadband E-O modulators without using any optical resonators. The energy consumption of typical silicon Mach–Zehnder interferometer modulators is a few pJ/bit.[29] Modulators using two-dimensional materials such as graphene consume energy at ~1.6 pJ/bit.[30] For III-V EA modulators, the energy consumption can be reduced to 608 fJ/bit.[31] Therefore, our EA modulators have better energy efficiency than most reported results. In addition, the energy efficiency of our device can be further improved using thinner HfO_2 and even higher mobility TCO materials such as CdO,[24] which will be investigated in our

future research. The total series resistance of the device is 27 kΩ, which mainly comes from the Si waveguide. Because the Hall measurement of the In_2O_3 film yielded an "ON" state resistivity of 0.0018 $\Omega \cdot$ cm, which is negligible compared to the high resistance of Si, the RC bandwidth can be improved by further increasing the doping level of the Si layer. If the doping concentration of Si layer can reach 1×10^{19} cm^{-3} and the segmented waveguide configuration can be replaced by an Si slab waveguide with 50-nm slab thickness, we will be able to reduce the series resistance to 111 Ω. In that case, the RC limited bandwidth may be improved to 12.5 GHz.

7 Conclusion

In conclusion, we have demonstrated a hybrid silicon-plasmonic EA modulator using high-mobility In_2O_3 as the gate. With an ultra-compact EA region of only 5 μm, we achieved a small voltage swing V_{pp} of 2 V to obtain an EA rate of 1.2 dB/μm, resulting in very high energy efficiency of 110 fJ/bit. In addition, the hybrid EA modulator is capable of covering more than 100-nm optical bandwidth in the telecommunication window and 55 MHz RC-delay limited bandwidth, which can be modulated at 2.5 GHz. Our work proves that In_2O_3-gated silicon-plasmonic EA modulators can play pivotal roles for future high density, high energy-efficiency on-chip optical interconnects.

Acknowledgments

References

1. N. Youngblood et al., "Multifunctional graphene optical modulator and photodetector integrated on silicon waveguides," *Nano Lett.* **14**(5), 2741–2746 (2014).
2. C. Y. Lin et al., "Electro-optic polymer infiltrated silicon photonic crystal slot waveguide modulator with 23 dB slow light enhancement," *Appl. Phys. Lett.* **97**(9), 194 (2010).
3. P. Markov et al., "Hybrid Si-VO$_2$-Au optical modulator based on near-field plasmonic coupling," *Opt. Express* **23**(5), 6878–6887 (2015).
4. E. Li et al., "Ultracompact silicon-conductive oxide nanocavity modulator with 0.02 lambda-cubic active volume," *Nano Lett.* **18**(2), 1075–1081 (2018).
5. E. Li et al., "One-volt silicon photonic crystal nanocavity modulator with indium oxide gate," *Opt. Lett.* **43**(18), 4429–4432 (2018).
6. Y. W. Huang et al., "Gate-tunable conducting oxide metasurfaces," *Nano Lett.* **16**(9), 5319–5325 (2016).
7. G. V. Naik, V. M. Shalaev, and A. Boltasseva, "Alternative plasmonic materials: beyond gold and silver," *Adv. Mater.* **25**(24), 3264–3294 (2013).
8. A. P. Vasudev et al., "Electro-optical modulation of a silicon waveguide with an 'epsilon-near-zero' material," *Opt. Express* **21**(22), 26387–26397 (2013).
9. M. Z. Alam, I. De Leon, and R. W. Boyd, "Large optical nonlinearity of indium tin oxide in its epsilon-near-zero region," *Science* **352**(6287), 795–797 (2016).
10. E. Feigenbaum, K. Diest, and H. A. Atwater, "Unity-order index change in transparent conducting oxides at visible frequencies," *Nano Lett.* **10**(6), 2111–2116 (2010).
11. G. V. Naik, J. Kim, and A. Boltasseva, "Oxides and nitrides as alternative plasmonic materials in the optical range," *Opt. Mater. Express* **1**(6), 1090–1099 (2011).
12. K. Shi and Z. Lu, "Field-effect optical modulation based on epsilon-near-zero conductive oxide," *Opt. Commun.* **370**, 22–28 (2016).
13. C. A. Neugebauer, L. I. Maissel, and R. Glang, *Handbook of Thin Film Technology*, Mcgraw Hill, New York (1970).
14. G. Giusti, "Deposition and characterisation of functional ITO thin films," PhD Thesis, University of Birmingham (2011).

15. B. H. Tahar et al., "Tin doped indium oxide thin films: electrical properties," *J. Appl. Phys.* **83**(5), 2631–2645 (1998).
16. H. Kim et al., "Epitaxial growth of Al-doped ZnO thin films grown by pulsed laser deposition," *Thin Solid Films* **420–421**, 107–111 (2002).
17. U. Koch et al., "Digital plasmonic absorption modulator exploiting epsilon-near-zero in transparent conducting oxides," *IEEE Photonics J.* **8**(1), 1–3 (2016).
18. A. V. Krasavin and A. V. Zayats, "Photonic signal processing on electronic scales: electro-optical field-effect nanoplasmonic modulator," *Phys. Rev. Lett.* **109**(5), 053901 (2012).
19. G. Sinatkas et al., "Transparent conducting oxide electro-optic modulators on silicon platforms: a comprehensive study based on the drift-diffusion semiconductor model," *J. Appl. Phys.* **121**(2), 23109 (2017).
20. H. W. Lee et al., "Nanoscale conducting oxide PlasMOStor," *Nano Lett.* **14**(11), 6463–6468 (2014).
21. V. J. Sorger et al., "Ultra-compact silicon nanophotonic modulator with broadband response," *Nanophotonics* **1**(1), 17–22 (2012).
22. M. G. Wood et al., "Gigahertz speed operation of epsilon-near-zero silicon photonic modulators," *Optica* **5**(3), 233–236 (2018).
23. Q. Gao, E. Li, and A. X. Wang, "Ultra-compact and broadband electro-absorption modulator using an epsilon-near-zero conductive oxide," *Photonics Res.* **6**(4), 277–281 (2018).
24. S. Campione et al., "Submicrometer epsilon-near-zero electroabsorption modulators enabled by high-mobility cadmium oxide," *IEEE Photonics J.* **9**(4), 1–7 (2017).
25. X. Xu et al., "Complementary metal–oxide–semiconductor compatible high efficiency subwavelength grating couplers for silicon integrated photonics," *Appl. Phys. Lett.* **101**(3), 031109 (2012).
26. A. Wettstein, A. Schenk, and W. Fichtner, "Quantum device-simulation with the density-gradient model on unstructured grids," *IEEE Trans. Electron Devices* **48**(2), 279–284 (2001).
27. Q. Gao, E. Li, and A. X. Wang, "Comparative analysis of transparent conductive oxide electro-absorption modulators," *Opt. Mater. Express* **8**(9), 2850–2862 (2018).
28. C. Hoessbacher et al., "The plasmonic memristor: a latching optical switch," *Optica* **1**(4), 198–202 (2014).
29. W. M. Green et al., "Ultra-compact, low RF power, 10 Gb/s silicon Mach–Zehnder modulator," *Opt. Express* **15**(25), 17106–17113 (2007).
30. S. Ren et al., "A Ge/SiGe quantum well waveguide modulator monolithically integrated with SOI waveguides," in *8th IEEE Int. Conf. Group IV Photonics*, pp. 11–13 (2011).
31. C. T. Phare et al., "Graphene electro-optic modulator with 30 GHz bandwidth," *Nat. Photonics* **9**(8), 511 (2015).

Biographies of the authors are not available.